Periodic three-dimensional mesh generation for particle reinforced composites with application to metal matrix composites

F. Fritzen *, T. Böhlke

Chair for Continuum Mechanics, Institute of Engineering Mechanics, Karlsruhe Institute of Technology (KIT), Kaiserstr. 10, D-76131 Karlsruhe, Germany

ARTICLE INFO

ABSTRACT

A method for the generation of three-dimensional model microstructures resembling particle reinforced composites is developed based on the periodic Voronoi tessellation. The algorithm allows for the generation of arbitrary particle volume fractions and produces periodic geometries based on the erosion procedure suggested by Christoffersen (1983). A technique for the creation of high quality periodic spatial discretizations of the particle systems for application with the finite element method is described in detail. The developed procedure is extensively applied to metal ceramic composites (Al-SiC$_p$) at volume fractions ranging from 10 to 80%. The elastic and thermo-elastic material properties are investigated and the effect of higher statistical moments (see, e.g., Torquato, 2002), i.e. of the particle shape and relative position, is evaluated in terms of constraint point sets used in the generation of the random microstructures.

© 2010 Elsevier Ltd. All rights reserved.

1. Introduction

The effective properties of heterogeneous materials are much sought-after quantities. In order to computationally predict the effective behavior of heterogeneous materials it is necessary to first find a precise topological description of the considered microstructure. Unfortunately, the acquisition of this information is hindered by a multitude of problems. A popular experimental technique is the serial sectioning using either polishing (Ganesh and Chawla, 2005) or the FIB (focus ion beam) technique (Groeber et al., 2006) combined with optical or electrical measurements. Another is the X-ray micro computer tomography (e.g., Madi et al., 2007). All these methods share a considerable sensitivity with respect to certain physical properties, e.g., electrical conductivity or the local mass density of the material. This renders the choice of a suitable experimental method a challenging procedure. Further, many of the mentioned techniques are destructive, i.e. they do only allow for limited (if any) in situ measurements, or for verification of the computed results (at least in the non-linear regime). When statistical studies with respect to different microstructures are aspired, then the effort for experimental techniques on the microstructural level is immense.

An efficient use of the limited amount of experimental data can be achieved by recourse to the statistical properties of the microscopic medium. The latter are, generally, determined by the n-point statistics of the material (see, e.g., Ohser and Mücklich, 2000; Torquato, 2002). For many composite structures additional simplified statistical measures exist, e.g., the distribution of the filament length in fibrous composites and the fiber orientation distribution function. Once this statistical data is collected, random variables can be used to evaluate numerous realizations of a virtual material. After generation of an adequate spatial discretization, the model structures can be used in computer based statistical studies. The Voronoi tessellation was found to be an efficient tool for the simulation of crystal aggregates (Kumar and Kurtz, 1994). Later, Decker and Jeulin (2000) introduced the concept of a periodic Voronoi tessellation for the use with artificial microstructures. Since, the periodic Voronoi tessellation has been applied to many microstructural problems with success (see, e.g., Barbe et al., 2001; Fritzen et al., 2009; Böhlke et al., 2010). Often the finite element method (FEM) (e.g., Zienkiewicz et al., 2006) is used in order to evaluate the mechanical and thermo-mechanical properties. The FEM requires a three-dimensional discretization of the microstructure. The construction of these discretizations from experimental data is still a challenging procedure for two-dimensional problems, see e.g., Yue et al. (2003), Prabu and Karunamoorthy (2008) or Reid et al. (2008), and often requires manual interactions. For the three-dimensional case, tools are currently being developed by various groups (Kim et al., 2002; Bhandari et al., 2007; Jang et al., 2008) for different classes of materials. The latter underlines the demand for efficient three-dimensional mesh generation methods. Therefore, the authors recently developed a generator for a particular class of periodic model microstructures based on the periodic

---

* Corresponding author. Tel.: +497216086904; fax: +497216084187.
E-mail addresses: fritzen@itm.uni-karlsruhe.de (F. Fritzen), boehlke@itm.uni-karlsruhe.de (T. Böhlke).
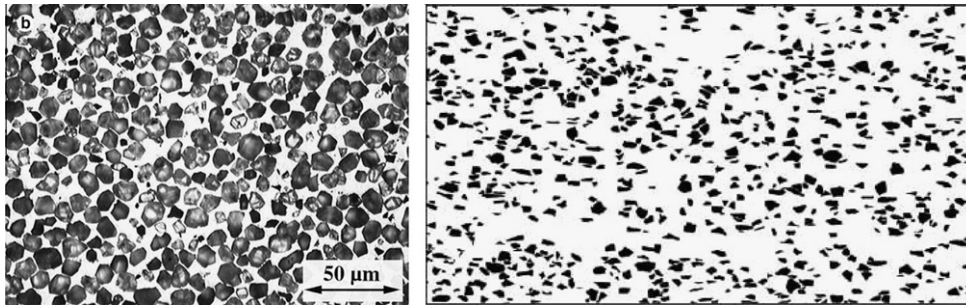
Fig. 1. Metal matrix composites examined by Miserez et al. (2004) (left: Al-58% vol. Al₂O₃) and by Chawla et al. (2006b)[1] (right: Al-20% vol. SiC$_p$).

Voronoi tessellation including an algorithm for the generation of a periodic volume mesh (Fritzen et al., 2009).

In this paper the technique is modified and adopted for consideration of particle-reinforced microstructures. Prominent examples for materials with such micromorphology are metal matrix composites such as the ones examined by Miserez et al. (2004), Ganesh and Chawla (2005) or Chawla et al. (2006c). These materials tempt to combine the thermal resistance and high stiffness of ceramic materials with the ductility observed for many metals. Comprehensive overviews on the topic are given by, e.g., Clyne and Withers (1995), Suresh (2002) and Chawla and Chawla (2006).

In order to overcome the afore mentioned experimental cost, a class of model microstructures based on the Voronoi tessellation is developed in Section 2. A similar approach to granular materials was initially suggested by Christoffersen (1983) in the context of geomaterials and for the use with analytic calculus. Here, a three-dimensional realization of the structure is addressed with the additional consideration of periodicity of the microstructure. The aim in this work is the development of sophisticated numerical tools for realistic simulations of such materials. The influence of different point seed parameters on the statistics of the effective response of the microstructures is investigated. The algorithm described by Fritzen et al. (2009) for the generation of periodic three-dimensional FEM discretizations of Voronoi tessellations is extended to the considered particle systems. A method for the generation of high-quality meshes for the particle model microstructures is presented in Section 3. The microstructures are applied to linear thermo-mechanical problems in Section 4. The influence of the mesh density on the effective thermo-mechanical material parameters is examined. Further, the isotropic material properties of the composite material are computed for different volume fractions. The study is repeated for constraint types of Voronoi tessellation and the resulting macroscopic material parameters are compared to the ones of the unconstrained tessellation.

2. Model microstructures for particulate materials

The scope of this paper are particulate materials, i.e. multiphase materials consisting of an interconnected phase (referred to as matrix material) and separated particles. Examples for such materials are Al-Al₂O₃ based metal matrix composites (Miserez et al., 2004) and Al/SiC$_p$ composites (Chawla et al., 2006a,b). While several investigations based on image recognition techniques applied to two-dimensional cross-sections of such materials have been used in FEM simulations recently (Figs. 1 and 2), three-dimensional discretizations are only sparsely used (Chawla et al., 2006c). More precisely, pseudo three-dimensional structures are often employed, e.g., the axi-symmetric cell employed by Doghri and Ouaar (2003), or the number of considered microstructures is small due to the excessive cost associated with the generation of the geometry and the meshes. This small number does not allow for statistical investigations.
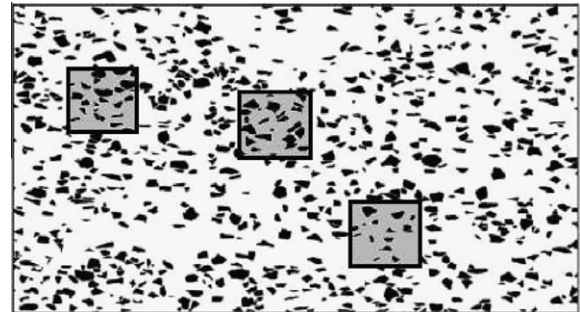

Fig. 2. Subdomains with near-homogeneous particle distribution (Chawla et al., 2006b)[1].

In order to find a class of suitable model microstructures, the following characteristic topological features of particulate metal matrix composites will be taken into account:

- The particles are mostly convex and often polygonal.
- The volume fraction of the particles is found to vary from very small values, e.g. 5%, up to values as large as 60% or more.
- While agglomerations of particles can sometimes be observed, the particles are often homogeneously distributed, particularly, if the volume fraction of particles is large (e.g., Fig. 1, left). For small and moderate total particle volume fractions, the composite often consists of domains with approximately homogeneous particle distribution, but with varying volume fraction. Thus, the properties of these almost homogeneous domains can be employed to reproduce the global material response.
- The particle size varies within a certain range. However, very large and very small grains are rarely observed. While the size distribution appears to be highly heterogeneous in two-dimensional micrographs, three-dimensional reconstructions (e.g. by Chawla et al. (2004)) show that the actual particle size varies in a moderate range.

Starting from a heuristic approach, the shape of the three-dimensional cells reconstructed by Chawla et al. (2004) is compared to the cells of a Voronoi tessellation (Fig. 4). It is observed that the shape of the SiC particles reconstructed by Chawla et al. (2004) is correlated to the polygonal shape of the cells in a Voronoi tessellation. Therefore, the following investigations are based on artificial microstructures generated using random Voronoi tessellations (see Aurenhammer, 1991 for a review). This allows for a large number of random realizations and, hence, allows for statistical studies based on Monte Carlo type simulations.

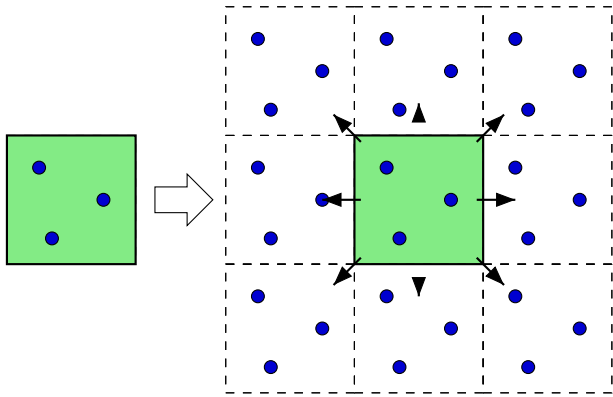For simplicity, we confine ourselves to the case of a cuboidal

Fig. 3. Periodization of the point seed.

unit cell $\Omega \in [-L/2, L/2] \times [-L/2, L/2] \times [-L/2, L/2]$. In a first step, N points (the Voronoi generators) are seeded randomly in the unit cell. These vertices are then copied 26 times around the unit cell in order to enforce periodicity of the Voronoi tessellation (Fig. 3) (Decker and Jeulin, 2000). The latter allows for the application of the favorable periodic displacement fluctuation boundary conditions in finite element computations, if the generated mesh is periodic, too. A tessellation resulting from this process is shown in Fig. 4.

In order to arrive at a particulate structure, the key idea in our approach is the erosion of the Voronoi cells by moving the cell walls homogeneously in inward normal direction by a given offset $w/2$ (Fig. 5). Such an erosion process is a common procedure in image processing where it can, e.g., be used in combination with dilatation processes to smoothen data (see, e.g., Ragnemalm, 1992). Our approach is, however, not based on an image based technique.

Between two neighboring particles a wall of thickness w is thereby created. All of the walls in the unit cell form an interconnected network resembling a closed cell foam as examined, e.g., by Roberts and Garboczi (2001). In our studies this structure is occupied by the matrix material. The described procedure has the following advantages:
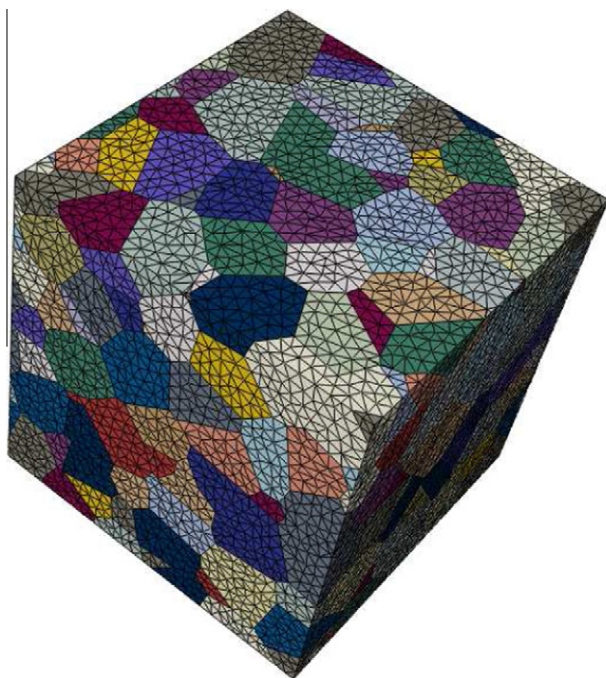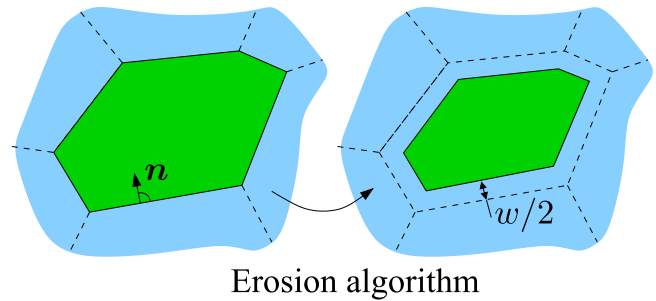

Erosion algorithm

Fig. 5. Schematical representation of the erosion algorithm for a single Voronoi cell.

- The distance between particles is (mostly) homogeneously distributed, unless originally small cells, which are deleted in the erosion process.
- The faces of neighboring particles are parallel.
- The volume fraction of the particles can be arbitrarily chosen. This is an advantage over many existing algorithms based on spherical, ellipsoidal or polygonal cells, which cannot be applied if the volume fraction of the particles is large. The method of simulated annealing was used by Flaquer et al. (2007) to produce virtual diamond ceramic microstructures to overcome this short-coming. However, the statistical properties of the microstructures generated in the process of simulated annealing are hard to predict.
- The number of cell faces of small particles is smaller than of large particles. This can account for the fact that small particles are often generated from larger particles by brittle cracking. The latter is exemplified in Fig. 6, where the number of faces of the particle P1 is significantly smaller than the one of particle P2.
- The properties of the microstructure can easily be modified by introduction of a minimum distance between two generator points (see, e.g., Fritzen et al., 2009). The latter is commonly referred to as hardcore condition. Another possibility is the generation of a centroidal Voronoi tessellation (Du et al., 1999) (Fig. 7).
  The cells generated using either of the two constraints are more regular, i.e. bad aspect ratios (Fig. 8) or small cells (Fig. 9) can be prevented. The particle shape can, hence, be controlled. Holding the particle volume fraction fixed, the effect of higher statistical moments on the effective properties of the material can, thus, be investigated.

3. Periodic mesh generation

3.1. Generation of the geometry

The generation of a periodic spatial discretization of the model microstructure described in Section 2 is subdivided into two major steps, (i) the generation of the geometry and (ii) the subsequent generation of a periodic surface and the derived volume mesh. The creation of the geometry can be enriched by an iterative algorithm in order to construct cells with a prescribed volume fraction (Section 3.2).
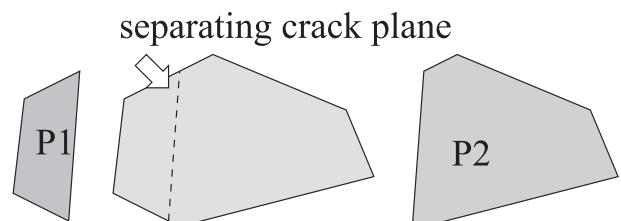

Fig. 4. Periodic Voronoi tessellation (200 grains).

separating crack plane

Fig. 6. Reduction of the number of particles faces due to brittle particle cracking.
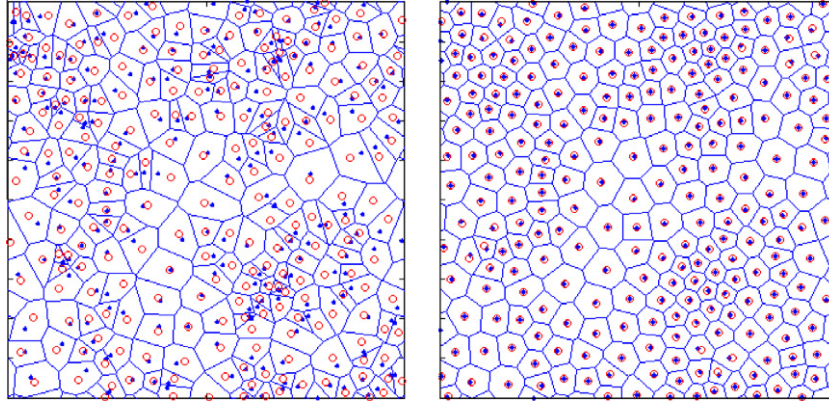
Fig. 7. Comparison of a random Voronoi tessellation (left) and the resulting centroidal Voronoi tessellation (right) after 5 iterations (50 Voronoi points); shown are the centers of mass and the Voronoi generators.
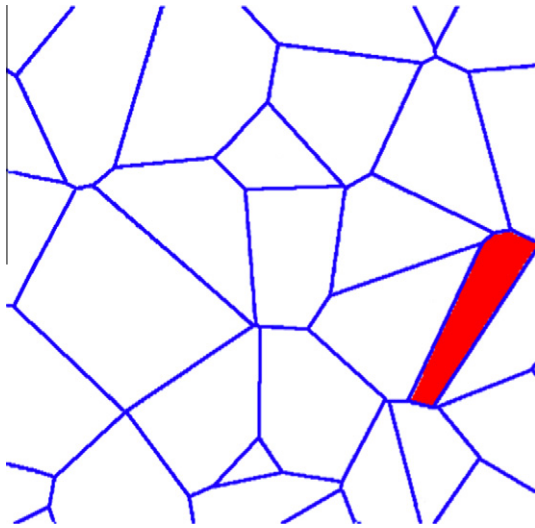

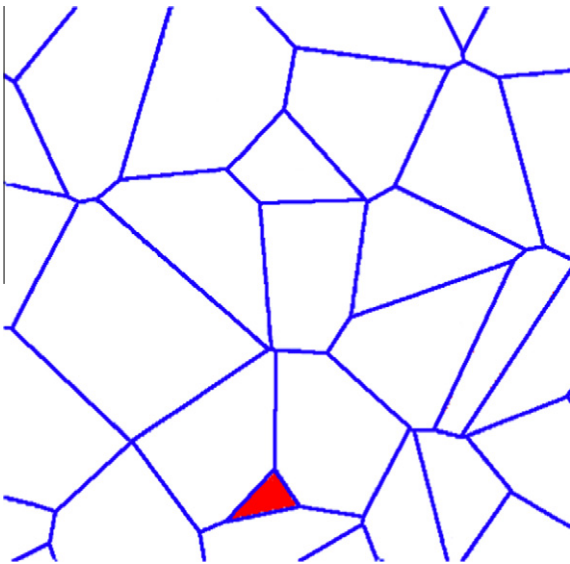**Fig. 8.** 2d Voronoi cell with high aspect ratio.

Fig. 9. Small cell in a 2d Voronoi tessellation.

In this section we focus on the generation of the geometry which, first, requires the creation of a random point seed containing the

Voronoi generators. As described in Section 2 the point seed may be subjected to different constraints. After the initial creation the vertices are copied around the unit cell (Fig. 3) to enforce a periodicity constraint and the Voronoi tessellation is generated using the `qhull` package (Barber et al., 1996). The output of the latter consists of a set of corner vertices for each Voronoi cell. Then each of these cells undergoes a erosion process, where only cells having a non-empty intersection with the unit cell are considered in order to increase the computational efficiency. The erosion process exploits the dual representation of the polyhedral (i.e. convex) cells in terms of the set $\mathscr{H}$ of n_H halfspaces,

$$\mathscr{H} = \{(\boldsymbol{n}_i, d_i) \in \mathbb{R}^3 \times \mathbb{R}\}, \tag{1}$$

which are defined in terms of the inward normal $\boldsymbol{n}_i$ and the normal distance from the origin d_i. Any point $\boldsymbol{x}$ found inside (or on the boundary) of the considered cell then satisfies the inequalities

$$\boldsymbol{n}_i \cdot \boldsymbol{x} + d_i \leqslant 0 \quad (i = 1, \dots, n_H). \tag{2}$$

In order to erode a polyhedral cell in inward normal direction, it suffices to modify the normal distance d_i of all separating hyperplanes via

$$d_i^* = d_i + h, \tag{3}$$

where h equals half of the wall thickness w separating two neighboring particles (Fig. 5). While the erosion algorithm itself is suggestive to be simple, the algorithmic realization involves elements of computational geometry and the associated algorithmic challenges. In our approach the program `qhalf` included in the `qhull` package was used in order to determine the corner points and the facet information of the eroded cell. It can calculate the cell in terms of the intersection of the set of modified halfspaces $\mathscr{H}^* = \{(\boldsymbol{n}_i, d_i^*)\}$. However, `qhalf` requires an interior point of the final eroded cell as additional input parameter. In particular, it has to be known a priori if the cell is deleted in the course of the process, due to its small initial size. The problem can be solved by first checking if the cell midpoint $\boldsymbol{m}$ is found inside of the final cell based on the inequalities (2) with d_i replaced by d_i^*. If this is the case then $\boldsymbol{m}$ is taken as interior point and one can proceed. Otherwise each of the n_H planes is treated individually in order to construct intermediate cells. The last intermediate cell then results in the final eroded cell, if the algorithm is not aborted due to deletion of the cell caused by the erosion process. The algorithm is initialized with the original cell. In each of the following iterations, the halfspace representation and the corner points of the intermediate cell $\mathscr{C}^{(j)}$ are needed. In the j-th step we define

$$d_i^{(j)} = \begin{cases} d_i & i > j, \\ d_i^* & i \leqslant j. \end{cases} \tag{4}$$

Then the intermediate corner point with the furthest normal distance to the plane $\left(\boldsymbol{n}_j, d_j^{(j)} \right)$ is identified by $\boldsymbol{p}^{(j)}$. If the distance δ of this point from the plane is negative, then the algorithm stops since the halfspace intersection results into an empty set. Otherwise, a truly interior point of the eroded cell is

$$\boldsymbol{q}^{(j)} = \boldsymbol{p}^{(j)} + \frac{\delta}{2}(\boldsymbol{m}^{(j)} - \boldsymbol{p}^{(j)}), \tag{5}$$

and the intersection computed based on this point defines the subsequent intermediate cell. After n_H steps the algorithm has produced the eroded cell, since $d^{(n_H)} = d_i^*$ holds. A schematic AI two-dimensional scheme of the algorithm is shown in Fig. 10. In the current work no particles were deleted, even if the volume of the particle was small (see, e.g., Fig. 10 rightmost picture). Many composite materials contain such small particles. If such small inclusions are not desired in the presented model, they can be deleted in the algorithm without additional cost.

After the erosion process, the modified cell is still not necessarily found inside of the considered unit cell. Hence, an intersection of the polyhedron with the cuboidal volume element has to be computed. The resulting geometric data, i.e. point coordinates, facet and cell information, is then used in the following mesh generation.

3.2. Particle volume fraction iteration

Before the actual mesh generation step, the volume fraction c_p of the particles is computed. Since the one point statistics (i.e. the volume fractions) of real materials can often be determined to a considerable precision, it is desirable to replicate certain given values of the particle volume fraction to the best possible extent. Therefore, we developed an iterative procedure that adjusts the cell wall thickness w automatically, until the desired volume fraction c_p^* is achieved. The following algorithm was found to produce fast convergence for (almost) arbitrary initial values, where a good initial guess for the wall thickness is

$w_0 = 2L(3/(4\pi N))^{1/3}\left(1 - c_p^{1/3}\right)$, which is derived from the assumption of spherical particles.

- V1 Initialize algorithm with $w = w_0 > 0$. Set $j = 0$.
- V2 Compute the eroded Voronoi tessellation and determine the volume fraction $c_p^{(j)}$. If $\left| c_p^{(j)} - c_p^* \right| < \epsilon$ accept the wall thickness and proceed with the mesh generation.
- V3 If $j < 3$ then set $w^{(j+1)} = \left(c_p^{(j)}/c_p^* \right)^{1/3} w^{(j)}$. Otherwise, determine $w^{(j+1)}$ by means of quadratic extrapolation from the previous three iterations. Set $j \rightarrow j + 1$ and proceed with [V2].

Examples illustrating the robustness of the algorithm, even for unfortunate initial guesses w_0, are shown in Table 1. The iteration time for all of the considered examples was below 60 seconds on a standard notebook computer. This highlightens the efficiency of the proposed algorithm.

3.3. Hierarchical mesh generation algorithm

The mesh generation procedure used for composite materials with particle reinforcement is related to the one developed by the authors previously for polycrystalline aggregates (Fritzen et al., 2009). A hierarchical meshing algorithm is applied in order to guarantee the periodicity of the resulting discretization. More precisely, after having determined the (periodic) geometric input, the corner points of the cells are the first mesh entities. In the next step all edges found on master surfaces, i.e. at $x = L/2$, $y = L/2$ or $z = L/2$, or inside of the unit cell are endowed with a point seed. Again, all mesh entities are held constant during the following steps, i.e. no points are inserted on any of the considered edges. Then, based on the fixed point seed on the boundary of internal and external faces, a quality surface mesh is generated using the `triangle` library developed by Shewchuk (1996). The thereby generated surface mesh is more complicated than the one of polycrystalline aggregates (Fritzen et al., 2009) in the sense that every particle intersecting the boundary produces a complicated mesh topology. In particular, the mesh associated with the matrix material on the faces of the cube contains *holes* (Fig. 11). The bounding
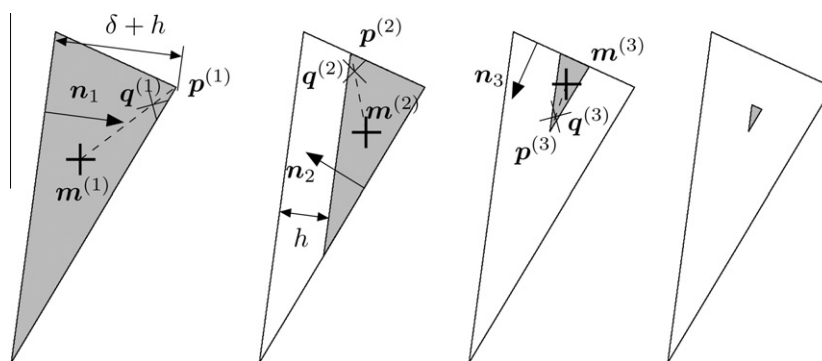
Fig. 10. Illustration of the subsequent erosion process.

Table 1
Results of the iteration process for prescribed volume fraction.

Vol. fraction	No. particles	$\left\| c_p^{(0)} - c_p^* \right\|(w_0)$	$w_{0/2}$	$n = n_{\text{vol.iter}}$	$\left\| c_p^n - c_p^* \right\|(w_n)$	$w_{n/2}$
20%	20	65.0%	0.01	8	0.00016%	0.07750
20%	20	19.6%	0.05	6	0.00170%	0.07750
20%	50	42.3%	0.02	9	0.00010%	0.05646
50%	50	12.3%	0.02	6	0.00066%	0.02817
80%	40	59.5%	0.06	9	0.00001%	0.01067

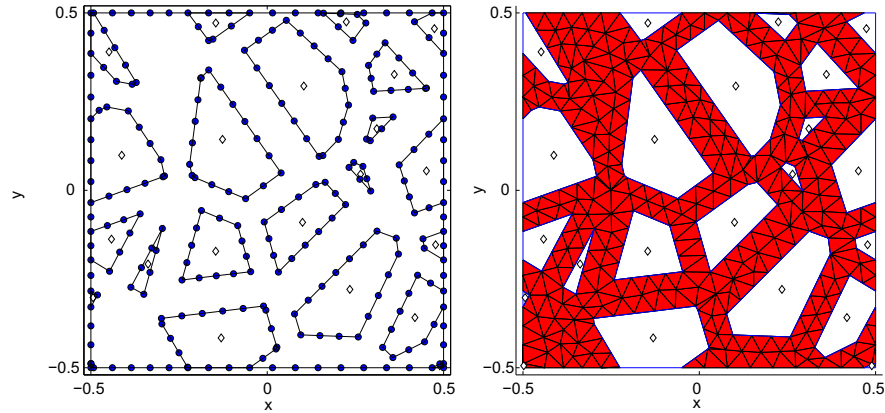**Fig. 11.** Surface mesh of the matrix material: Input data for the 2d mesh generator (left; ◇ represent hole indicators) and obtained surface mesh (right).

edge points of these have to conform with the surface mesh of the particles (and vice versa). Similar to the approach pursued for the crystalline aggregates (Fritzen et al., 2009), the mesh density can be controlled independently without introduction of geometrical imperfections. The latter property allows for the consideration of rather coarse meshes for quick estimates (see also Section 4.2). Moreover, a modified mesh density can be realized within the particles. This can help to reduce the number of degrees of freedom in calculations with, e.g., elastic particles and an elasto-plastic matrix material.

All particle faces are meshed independently and the resulting surface meshes are merged into the final surface mesh of the microstructure. In the last step of the mesh generation procedure this surface mesh is used as input data for the popular tetgen (Si and Gaertner, 2005) mesh generator. Note that all surface mesh entities have to be fixed during the extrusion of the volume mesh in order to maintain the enforced periodicity. Finally, the mesh is converted and written into input files for ABAQUS/STANDARD and for a self-written three-dimensional finite element implementation. The latter is particularly designed for the purpose of computational homogenization in the presence of periodic displacement fluctuation conditions. The solution of the resulting linear systems of equations is performed using the preconditioned iterative solvers ILUPACK http://www-public.tu-bs.de (Bollhoefer and Saad, 2006) and HIPS http://hips.gforge.inria.fr. Some example meshes for different volume fractions are shown in Fig. 12.

4. Effective properties of Al-SiC_p

4.1. Problem setup

In the following, the elastic and thermo-elastic properties of Al-SiC$_p$ are examined in terms of virtual experiments. Periodic displacement fluctuation boundary conditions are assumed, i.e. the total displacement field $\boldsymbol{u}$ is additively decomposed into a homogeneous part $\boldsymbol{u}_h = \bar{\boldsymbol{\varepsilon}}\boldsymbol{x}$ and a fluctuation part $\tilde{\boldsymbol{u}}$

$$\boldsymbol{u} = \bar{\boldsymbol{\varepsilon}}\boldsymbol{x} + \tilde{\boldsymbol{u}}. \tag{6}$$

In order to replicate the prescribed kinematic loading $\bar{\boldsymbol{\varepsilon}}$, the fluctuation part $\tilde{\boldsymbol{u}}$ has to satisfy

$$\tilde{\boldsymbol{u}}(\boldsymbol{x}_+) = \tilde{\boldsymbol{u}}(\boldsymbol{x}_-) \tag{7}$$

for all boundary nodes $\boldsymbol{x}_+$ and $\boldsymbol{x}_-$ of the spatial discretization, that are found on opposing faces of the considered cuboidal unit cell (see Fig. 13).

For a given displacement field $\boldsymbol{u}$ the infinitesimal strain tensor $\boldsymbol{\varepsilon}$ is defined via

$$\boldsymbol{\varepsilon} = \frac{1}{2}(\text{grad}(\boldsymbol{u}) + \text{grad}(\boldsymbol{u})^\top). \tag{8}$$

The local thermo-kinematical loading of a material from a stress-free equilibrium state is then described by the strain tensor $\boldsymbol{\varepsilon}$ and the temperature increment $\Delta\theta$. The latter is considered homogeneous within the unit cell due to the assumed separation of scales (e.g., Willis, 1981). In a linear elastic context the stress tensor $\boldsymbol{\sigma}$ induced by such thermo-kinematical loading is

$$\boldsymbol{\sigma} = \mathbb{C}[\boldsymbol{\varepsilon} - \boldsymbol{\alpha}\Delta\theta], \tag{9}$$

with the symmetric tensorial thermal expansion coefficient $\boldsymbol{\alpha}$ and the symmetric and positive definite material stiffness tensor $\mathbb{C}$. The elastic stiffness tensor and the tensorial thermal expansion coefficient both depend on the position $\boldsymbol{x}$, i.e., they are both heterogeneously distributed.

For each unit cell a total of seven different linear elastic boundary value problems are solved. The first six calculations serve to identify the elastic behaviour in the absence of thermo-elastic effects. Therefore, an orthonormal basis of the space of symmetric
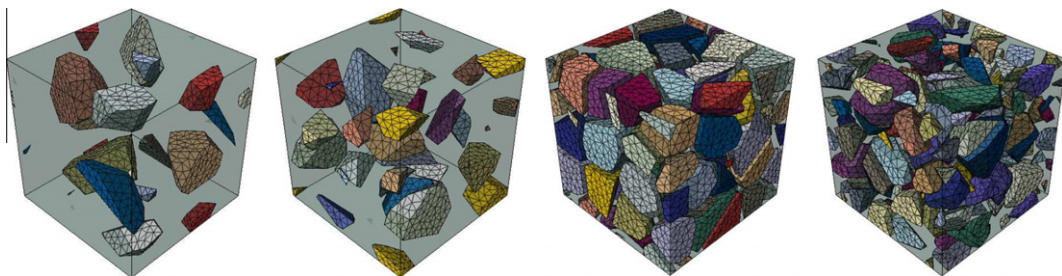

Fig. 12. Meshes containing 10, 20, 50 and 100 particles (10%, 10%, 60%, 30%).
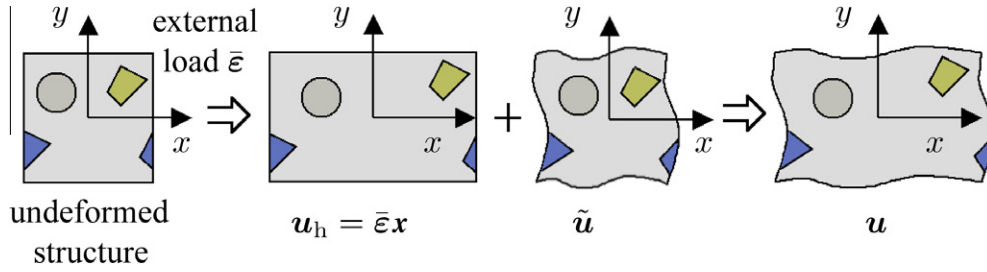
Fig. 13. Periodic displacement fluctuation boundary conditions.

tensors B_γ ($\gamma = 1,\dots,6$) is defined (e.g. Federov, 1968). These basis tensors are then used as boundary data, i.e. the boundary value problem

$$\text{div}(\mathbb{C}[\varepsilon_\gamma]) = \text{div}(\sigma_\gamma) = \mathbf{0} \quad \text{in} \quad \Omega, \qquad \langle \varepsilon_\gamma \rangle = B_\gamma \tag{10}$$

is solved for $\gamma = 1,\dots,6$. The six orthonormal basis tensors are

$$B_1 = e_1 \otimes e_1, \qquad\qquad B_2 = e_2 \otimes e_2, \tag{11}$$

$$B_3 = e_3 \otimes e_3, \qquad\qquad B_4 = \frac{\sqrt{2}}{2}(e_1 \otimes e_2 + e_2 \otimes e_1), \tag{12}$$

$$B_5 = \frac{\sqrt{2}}{2}(e_1 \otimes e_3 + e_3 \otimes e_1), \qquad B_6 = \frac{\sqrt{2}}{2}(e_2 \otimes e_3 + e_3 \otimes e_2). \tag{13}$$

Here, $\langle \bullet \rangle$ denotes the volume average of a quantity $\bullet$ over the unit cell. The solutions to these six problems define the apparent macroscopic stiffness $\widehat{\mathbb{C}}$ and the strain localization operator $\mathbb{A}$ of the considered micro-heterogeneous structure by

$$\widehat{\mathbb{C}} = \sum_{\gamma=1}^{6} \langle \sigma_\gamma \rangle \otimes B_\gamma, \qquad \mathbb{A} = \sum_{\gamma=1}^{6} \varepsilon_\gamma \otimes B_\gamma. \tag{14}$$

The linear operator $\mathbb{A}$ determines the microscopic strain tensor for a given macroscopic deformation according to

$$\varepsilon(\mathbf{x}) = \mathbb{A}(\mathbf{x})[\bar{\varepsilon}]. \tag{15}$$

Here and thereafter apparent quantities $\widehat{\bullet}$, e.g. the stiffness $\widehat{\mathbb{C}}$ of a particular realization of the model microstructure, are distinguished from effective quantities $\bar{\bullet}$, e.g. the effective stiffness $\overline{\mathbb{C}}$ of an infinite piece of material. The thermo-elastic interactions are considered in the seventh computation, which is defined by an eigenstress problem induced by a homogeneous temperature increment $\Delta\theta$

$$\text{div}(\mathbb{C}[\varepsilon_\theta - \Delta\theta\alpha]) = \text{div}(\sigma_\theta) = \mathbf{0} \quad \text{in } \Omega, \qquad \langle \varepsilon_\theta \rangle = \mathbf{0}. \tag{16}$$

The apparent tensorial thermal expansion coefficient $\hat{\alpha}$ of the material can be computed from the macroscopic compliance $\widehat{\mathbb{S}} = \widehat{\mathbb{C}}^{-1}$ and the thermally induced stress field σ_θ via

$$\hat{\alpha} = -\frac{1}{\Delta\theta}\widehat{\mathbb{S}}[\langle \sigma_\theta \rangle]. \tag{17}$$

In the following, the microscopic material parameters for the aluminum matrix and the silicon carbide particles of Chawla et al. (2006a) (Table 2) are assumed. Notably the parameters used here are representative for many other particle reinforced Al composites.

Table 2
Isotropic microscopic material parameters for the matrix and inclusion material (cf. Chawla et al., 2006a).

	E [GPa]	ν [-]	α [10^{-6} K^{-1}]
Al	70	0.33	25
SiC$_p$	400	0.19	4.3

4.2. Mesh density study

A mesh density study was carried out in order to investigate the influence of the chosen spatial resolution of the discretization onto the calculated material properties. Three different ensembles were investigated:

- 10% particle volume fraction based on 10 Voronoi generators,
- 20% particle volume fraction based on 20 Voronoi generators and
- 30% particle volume fraction based on 20 Voronoi generators.

For each of these ensembles eight different spatial discretizations of the same geometry are generated. The coarsest mesh contains approximately 20000 degrees of freedom in contrast to approximately 1100000 degrees of freedom for the finest discretization. Three of the eight considered discretizations for the ensemble based on 10 Voronoi generators are shown in Fig. 14.

The finest discretization containing more than one million degrees of freedom was chosen as reference solution. In order to quantify the deviation from this reference solution, three non-dimensional measures are introduced. For each mesh density level h_i, the smallest and the largest eigenvalue of $\widehat{\mathbb{C}}_{h_7}^{-1}\widehat{\mathbb{C}}_{h_i}$ quantify the deviation of the purely mechanical behaviour, while $\|\hat{\alpha}_{h_i} - \hat{\alpha}_{h_7}\|/\|\hat{\alpha}_{h_7}\|$ determines the difference in the tensorial apparent thermal expansion coefficient. The results for 10, 20 and 30% are shown in Tables 3–5.

For all considered ensembles, the apparent stiffness tensor tends to larger eigenvalues for coarser discretization levels, i.e. to a stiffer macroscopic material response. Taking into consideration the formulation of the apparent thermal expansion (17) and the stiffer apparent elasticity tensor, the lower thermal expansion coefficient found for coarser discretizations can be explained. However, the differences for coarser meshes are almost negligible (Tables 3–5). The smallest eigenvalue of the stiffness tensor is almost independent of the mesh density, too.

In the course of the mesh study we have found that for approximately 100000 mesh nodes, the relative error is in the order of 0.5 % and smaller for all three error measures. This deviation is considered acceptable and the meshes employed in all subsequent investigations all consist of approximately 100000 nodes, which is equivalent to 300000 degrees of freedom.

4.3. Influence of the particle volume fraction

The presented mesh generation technique has the favourable property of being able to generate model microstructures with arbitrary prescribed particle volume fraction (Section 3). In this section the influence of the amount of ceramic material on the effective thermo-elastic behaviour is evaluated for volume fractions of 10, 30, 50, 70 and 80%. This implies that no fluctuations of the volume fraction around the indicated values are considered. Examples of spatial discretizations for 50 and 80% volume fraction
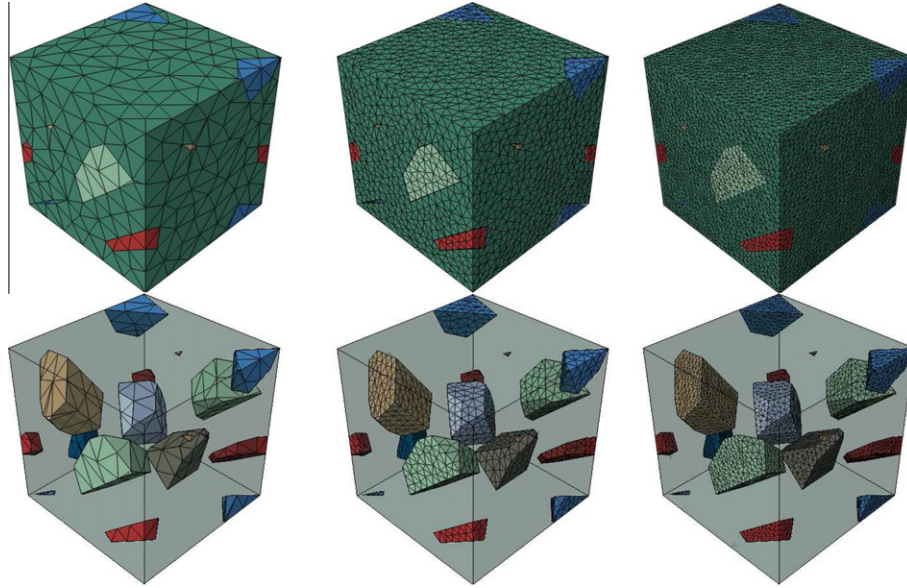
Fig. 14. Different discretization levels h_0 (left), h_3 (middle) and h_7 (right) for 10 particles (10% vol. frac.).

Table 3
Comparison of mesh densities for 10% particle volume fraction (10 Voronoi generators).

Mesh level	h_0	h_1	h_2	h_3	h_4	h_5	h_6	h_7
# Nodes	6502	11384	21024	40531	79258	158529	236590	363808
$\lambda_{\max}(\widehat{\mathbb{C}}_{h_7}^{-1}\widehat{\mathbb{C}}_{h_i}) - 1$ [%]	0.8768	0.5844	0.3472	0.2066	0.1123	0.0512	0.0230	–
$\lvert t\lambda_{\min}(\widehat{\mathbb{C}}_{h_7}^{-1}\widehat{\mathbb{C}}_{h_i}) - 1\rvert$ [%]	0.1687	0.1103	0.0669	0.0396	0.0211	0.0093	0.0042	–
$\lVert\hat{\boldsymbol{\alpha}}_{h_i} - \hat{\boldsymbol{\alpha}}_{h_7}\rVert/\lVert\hat{\boldsymbol{\alpha}}_{h_7}\rVert$ [%]	0.2172	0.1430	0.0870	0.0522	0.0279	0.0126	0.0062	–

Table 4
Comparison of mesh densities for 20% particle volume fraction (20 Voronoi generators).

Mesh level	h_0	h_1	h_2	h_3	h_4	h_5	h_6	h_7
# Nodes	10626	14363	22909	41385	79191	155374	232162	357520
$\lambda_{\max}(\widehat{\mathbb{C}}_{h_7}^{-1}\widehat{\mathbb{C}}_{h_i}) - 1$ [%]	2.0628	1.4782	0.7912	0.4907	0.2630	0.1147	0.0529	–
$\lvert\lambda_{\min}(\widehat{\mathbb{C}}_{h_7}^{-1}\widehat{\mathbb{C}}_{h_i}) - 1\rvert$ [%]	0.4217	0.2908	0.1654	0.0991	0.0519	0.0234	0.0108	–
$\lVert\hat{\boldsymbol{\alpha}}_{h_i} - \hat{\boldsymbol{\alpha}}_{h_7}\rVert/\lVert\hat{\boldsymbol{\alpha}}_{h_7}\rVert$ [%]	0.5378	0.3742	0.2108	0.1265	0.0664	0.0299	0.0142	–

Table 5
Comparison of mesh densities for 30% particle volume fraction (20 Voronoi generators).

Mesh level	h_0	h_1	h_2	h_3	h_4	h_5	h_6	h_7
# Nodes	10150	13649	23257	40179	77729	152091	228745	354322
$\lambda_{\max}(\widehat{\mathbb{C}}_{h_7}^{-1}\widehat{\mathbb{C}}_{h_i}) - 1$ [%]	2.3906	1.9991	1.1268	0.5878	0.3335	0.1396	0.0612	–
$\lvert\lambda_{\min}(\widehat{\mathbb{C}}_{h_7}^{-1}\widehat{\mathbb{C}}_{h_i}) - 1\rvert$ [%]	0.4493	0.3684	0.1976	0.1143	0.0606	0.0256	0.0116	–
$\lVert\hat{\boldsymbol{\alpha}}_{h_i} - \hat{\boldsymbol{\alpha}}_{h_7}\rVert/\lVert\hat{\boldsymbol{\alpha}}_{h_7}\rVert$ [%]	0.5907	0.4835	0.2633	0.1501	0.0796	0.0338	0.0153	–

are shown in Fig. 15. The realization of such high particle volume fractions is often a challenging problem requiring complicated techniques such as simulated annealing (Nogales and Böhm, 2008) and others. The algorithm presented in this contribution can, however, easily be triggered to provide the desired volume fractions without additional computational cost.

The microstructures generated for the particle volume fraction study are based on 20 Voronoi generators. For each volume fraction a total of 50 different realizations were computed, i.e. 250 different meshes were generated. The different realizations allow for basic Monte Carlo type statistical studies. The apparent bulk modulus $\widehat{K}$, shear modulus $\widehat{G}$ and isotropic thermal expansion coefficient $\hat{\alpha}$ of each realization were computed by isotropic projection

$$\widehat{K} = \frac{1}{3}\mathbb{P}_1^{\mathrm{iso}}\cdot\widehat{\mathbb{C}}, \qquad \widehat{G} = \frac{1}{10}\mathbb{P}_2^{\mathrm{iso}}\cdot\widehat{\mathbb{C}}, \qquad \hat{\alpha} = \frac{1}{3}\boldsymbol{I}\cdot\hat{\boldsymbol{\alpha}}, \tag{18}$$

with the identity on spherical tensors $\mathbb{P}_1^{\mathrm{iso}}$, deviatoric tensors $\mathbb{P}_2^{\mathrm{iso}}$ and the second order identity tensor $\boldsymbol{I}$. The arithmetic means of $\widehat{K}$ and $\widehat{G}$ are considered as the effective moduli $\overline{K}, \overline{G}$ and the standard deviation $\sigma(\widehat{G}), \sigma(\widehat{K})$ can be used to determine a confidence interval for the effective elastic response when assuming approximately a Gaussian distribution. Due to the observations by Kanit et al. (2003, 2006), the consideration of a larger number of small unit cells gives accurate predictions for the effective behaviour obtained from very large unit cells. This result is explicitly used here in order to derive the effective response of a material from a set of apparent
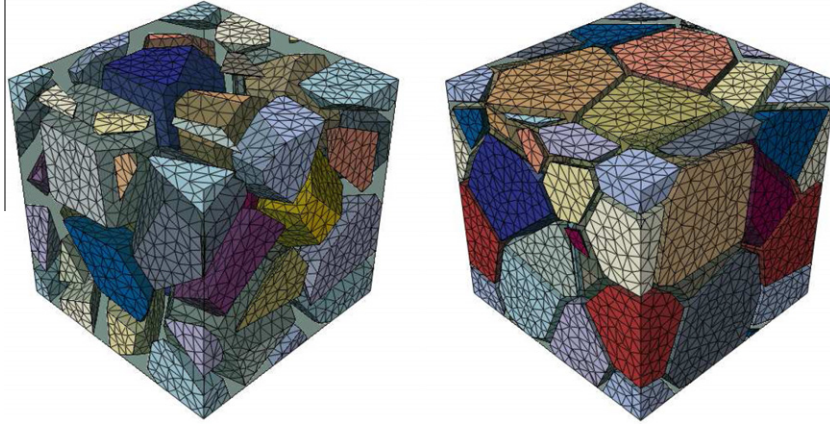
Fig. 15. Examples for 50% (left) and 80% (right) particles (≈100000 nodes).

properties. The effective isotropic thermal expansion $\bar{\alpha}$ and its standard deviation $\sigma(\hat{\alpha})$ are defined accordingly. A summary of the results is plotted in Fig. 16. For the three quantities $\bar{K}, \bar{G}$ and $\bar{\alpha}$ the first- and second-order bounds are also presented. The first-order bounds of $\bar{K}$ and $\bar{G}$ are the arithmetic and the harmonic mean of the corresponding phase properties. They are only based on the one-point correlation function, i.e. the volume fraction information. The Hashin-Shtrikman bounds (Willis, 1981) are of second order and take into account the one- and the two-point information of the microstructure. Here, the two-point statistics are assumed isotropic in accordance with the average particle shape.

The bounds for the thermal expansion coefficient are based on the explicit formulae for the localization tensors in two-phase composites which allow for a direct computation of first- and second-order bounds in terms of the corresponding elasticities. Furthermore, the self-consistent estimate of both, the elastic constants and the thermal expansion are also presented. The results computed by the finite element method are found to be close to the lower Hashin-Shtrikman bound for all particle volume fractions.

The numerical values are presented in Table 6 including a 3σ confidence interval. Further, the Young's modulus E and the Poisson ratio v can be computed from the bulk and shear modulus by

$$E(K, G) = \frac{9KG}{3K + G}, \qquad v(K, G) = \frac{1}{2}\frac{3K - 2G}{3K + G}. \qquad (19)$$

Based on the truncated Taylor expansions

$$E(\bar{K} + \delta K, \bar{G} + \delta G) \approx E(\bar{K}, \bar{G}) + \partial_K E(\bar{K}, \bar{G})\delta K + \partial_G E(\bar{K}, \bar{G})\delta G, \qquad (20)$$

$$v(\bar{K} + \delta K, \bar{G} + \delta G) \approx v(\bar{K}, \bar{G}) + \partial_K v(\bar{K}, \bar{G})\delta K + \partial_G v(\bar{K}, \bar{G})\delta G, \qquad (21)$$

an approximation of the respective standard deviations is given by

$$\sigma(E) \approx \sqrt{(\partial_K E(\bar{K}, \bar{G}))^2 \sigma^2(\hat{K}) + (\partial_G E(\bar{K}, \bar{G}))^2 \sigma^2(\hat{G})}, \qquad (22)$$

$$\sigma(v) \approx \sqrt{(\partial_K v(\bar{K}, \bar{G}))^2 \sigma^2(\hat{K}) + (\partial_G v(\bar{K}, \bar{G}))^2 \sigma^2(\hat{G})}. \qquad (23)$$

Notably, the first order approximations hold for small deviations $\sigma(\hat{K}), \sigma(\hat{G})$ only. In the results presented in Table 6 it can be seen that this assumption holds for all considered volume fractions.
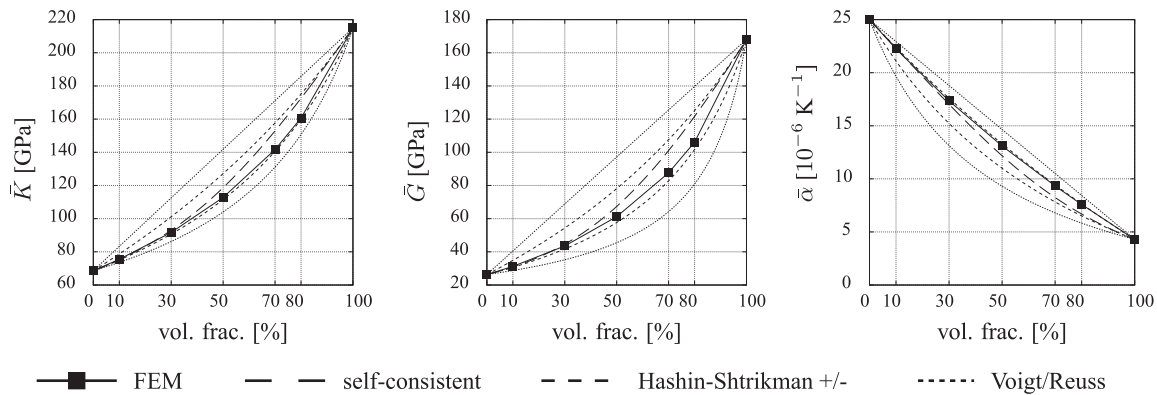

Fig. 16. Effective bulk modulus, shear modulus and thermal expansion coefficient vs. particle volume fraction.

Table 6
Effective isotropic thermo-elastic material parameters and 3σ confidence intervals for Al-SiC$_p$ at different particle volume fractions.

Vol. frac.	10%	30%	50%	70%	80%
$\bar{K}$ [GPa]	75.50 ± 0.125	91.72 ± 0.226	112.8 ± 0.282	141.7 ± 0.274	160.7 ± 0.193
$\bar{G}$ [GPa]	31.21 ± 0.124	43.54 ± 0.199	61.18 ± 0.267	87.60 ± 0.347	106.1 ± 0.346
$\bar{E}$ [GPa]	82.29 ± 0.288	112.8 ± 0.446	155.4 ± 0.578	217.9 ± 0.719	260.9 ± 0.700
$\bar{v}$ [10^{-2}]	31.83 ± 0.069	29.51 ± 0.092	27.03 ± 0.098	24.37 ± 0.094	22.93 ± 0.077
$\bar{\alpha}$ [10^{-6}K^{-1}]	22.23 ± 0.046	17.35 ± 0.056	13.10 ± 0.044	9.328 ± 0.029	7.585 ± 0.018

The Hashin-Rosen relation (Rosen and Hashin, 1970)

$$\bar{\alpha} = (1 - c_\mathrm{p})\alpha_\mathrm{m} + c_\mathrm{p}\alpha_\mathrm{p} + \frac{\alpha_\mathrm{m} - \alpha_\mathrm{p}}{K_\mathrm{m}^{-1} - K_\mathrm{p}^{-1}}\left(\frac{1}{\bar{K}} - \frac{1 - c_\mathrm{p}}{K_\mathrm{m}} - \frac{c_\mathrm{p}}{K_\mathrm{p}}\right). \qquad (24)$$

was used to verify the finite element implementation used for the effective thermal expansion coefficient based on the result of the elastic homogenization. While (24) is an exact representation for isotropic two phase materials, the computational approach based on (17) can be applied to systems containing arbitrarily anisotropic materials and an arbitrary number of different constituents, including voids. Additionally, the formulation (17) can be used to computed the apparent expansion coefficient $\hat{\alpha}$ without the need of an additional linear-elastic homogenization procedure. The preceeding formula was used to derive the thermal expansion coefficients derived from the Hashin-Shtrikman bounds, the Voigt and Reuss estimate and the self-consistent approximation.

4.4. Influence of the type of Voronoi tessellation

In this section the influence of the type of Voronoi tessellation on the effective thermo-elastic behaviour is investigated. Three different types of Voronoi tessellation are considered: (i) the standard Voronoi tessellation (SV) defined by a random (unconstrained) set of Voronoi generators, (ii) the hardcore Voronoi tessellation (HV) where the minimum distance between Voronoi generators is constraint and (iii) the centroidal Voronoi tessellation (CV). In the latter the center of each Voronoi cell coincides with the associated Voronoi vertex. By manipulation of the point seed at constant volume fraction, the effect of higher statistical moments on the properties of particulate structures can be evaluated. The latter aspect is illustrated in Fig. 17 by a top view comparing the periodic geometry

of a standard and a centroidal realization (30 vol.%, 20 generators). The geometry resulting from constraint point seed shows a pronounced increase in regularity of the particle shape, while the amount of ceramic material is identical in both cases. In the following, the subscript index SV denotes the standard tessellation, HV followed by a radius indicates the hardcore constraint and CV identifies quantities associated with the centroidal type of tessellation.

The study is carried out for particle volume fractions of 10, 30, 50, 70 and 80% and for a geometry based on a total of 20 Voronoi generators. For the hardcore condition the minimum point distances 0.15 and 0.20 relative to the length of the unit cell are investigated. For each of the five volume fractions and for each of the three different types of tessellation (two hardcore and one centroidal tessellation) 30 different random realizations are computed. In addition to these results, the existing data from Section 4.3 is used to compare the results to the ones of unconstraint point sets. The resulting additional 450 different unit cells are again each subjected to the seven load cases described earlier.

The effective isotropic elastic bulk and shear moduli $\bar{K}, \bar{G}$ of the different realizations and their standard deviations are computed. The values of the constraint tessellations are normalized with respect to the values of the unconstrained point seed (Fig. 18).

First, it can be observed that the effective isotropic material response is almost invariant with respect to changes of statistical moments of second and higher order. It is found that the bulk modulus of the regularized tessellations is smaller than the one of unconstrained tessellations. Notably the centroidal Voronoi tessellation has a significantly more pronounced impact than the hardcore condition. The qualitative change in value of the shear modulus is found to depend on the volume fraction. For small particle volume fractions, the increased regularity of the structure leads to matrix dominated, i.e. softer, material response. For high
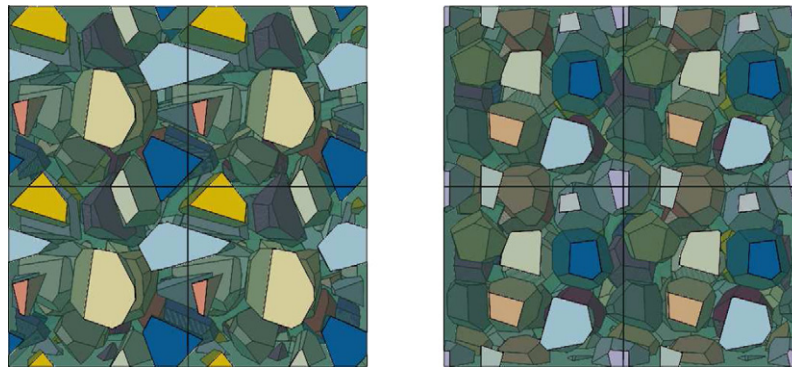

Fig. 17. Comparison of the microstructures resulting from a standard tessellation (left) and a centroidal tessellation (right) (translucent matrix material).
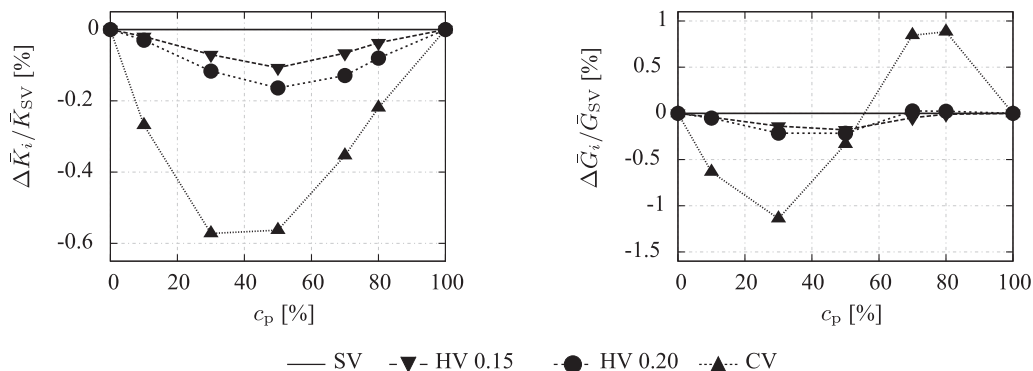

Fig. 18. Comparison of the normalized deviation of the effective bulk $(\bar{K}_i - \bar{K}_\mathrm{SV})/\bar{K}_\mathrm{SV}$ and shear modulus $(\bar{G}_i - \bar{G}_\mathrm{SV})/\bar{G}_\mathrm{SV}$ for the different tessellations (HV0.15, HV0.20, CV) (left: bulk modulus K, right: shear modulus G) as a function of the particle volume fraction c_p.

particle volume fractions the influence of the particle reinforcement is more pronounced than for the standard tessellation, i.e. a high modulus is found.

The second observation made in the course of the numerical study is a strong influence of the type of tessellation on the standard deviation of the effective material properties (Fig. 19). The increased regularity of the centroidal tessellation leads to a relative reduction in the standard deviation of up to 80%. The hardcore constraint resulted in a reduction of the statistical scatter for most volume fractions. However, the reduction was less distinct.

Additionally, the isotropic thermal expansion coefficient was evaluated. The values normalized with respect to the coefficient obtained from the unconstrained point seeds are shown in Fig. 20. The observed behaviour was almost identical to the one of the bulk modulus.

If not only the isotropic projection of the material properties is of interest a suitable measure of the induced macroscopic anisotropy is

$$\mathscr{A}(\mathbb{C}) = \frac{\lambda_{\max}(\mathbb{C}_{\text{iso}}^{-1}\mathbb{C})}{\lambda_{\min}(\mathbb{C}_{\text{iso}}^{-1}\mathbb{C})}, \tag{25}$$

with $\mathbb{C}_{\text{iso}} = 3\overline{K}\mathbb{P}_1^{\text{iso}} + 2\overline{G}\mathbb{P}_2^{\text{iso}}$. This anisotropy measure has been evaluated for the different types of tessellation and the different volume fractions in Fig. 21. While the two different hardcore conditions have a small effect on the amount of microstructural anisotropy, the centroidal type of tessellation reduces the directional dependency by more than 50 % over the standard tessellation.
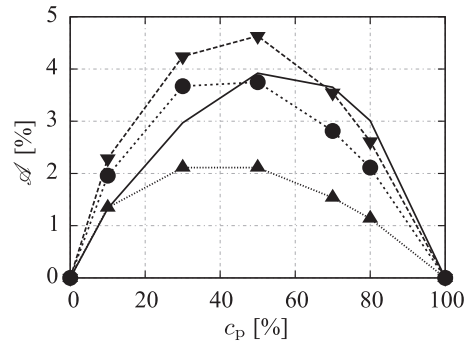

Fig. 21. Amount of macroscopic elastic anisotropy induced by the microstructured material.

4.5. Applications to other materials

In the previous applications the phase contrast in the Young's modulus E_p/E_m was approximately six which is an important ratio for metal ceramic composite materials with aluminium matrix. The authors would like to point out the possibility to use the proposed mesh generation method for the investigation of the properties of high contrast materials, e.g. for $E_p/E_m \approx 100$. In particular, the bounds and estimates provided by semi-analytical methods are often found in a broad range and full field simulations are indispensable, if more accurate predictions are required. The proposed computational method has been applied to the same microstructure but with two different sets of elastic constants to high-lighten
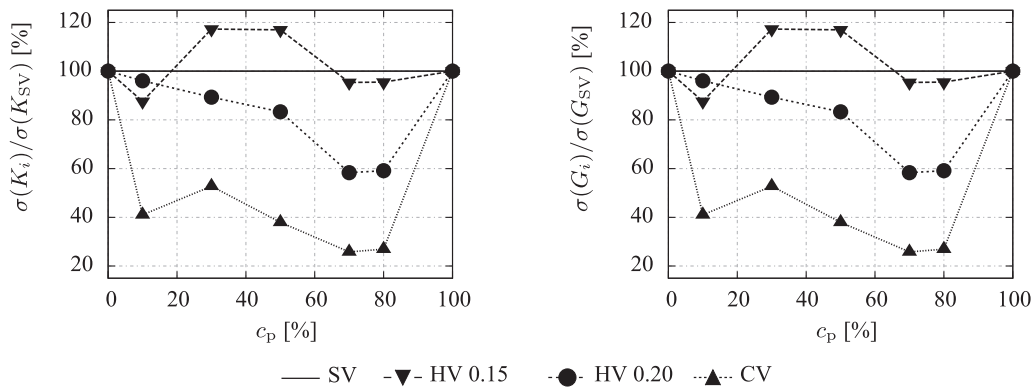

Fig. 19. Comparison of the normalized standard deviations of bulk modulus $\sigma(K_i)/\sigma(K_{\text{SV}})$ (left) and shear modulus $\sigma(G_i)/\sigma(G_{\text{SV}})$ (right) for tessellation types HV0.15, HV0.20, CV over particle volume fraction c_p.
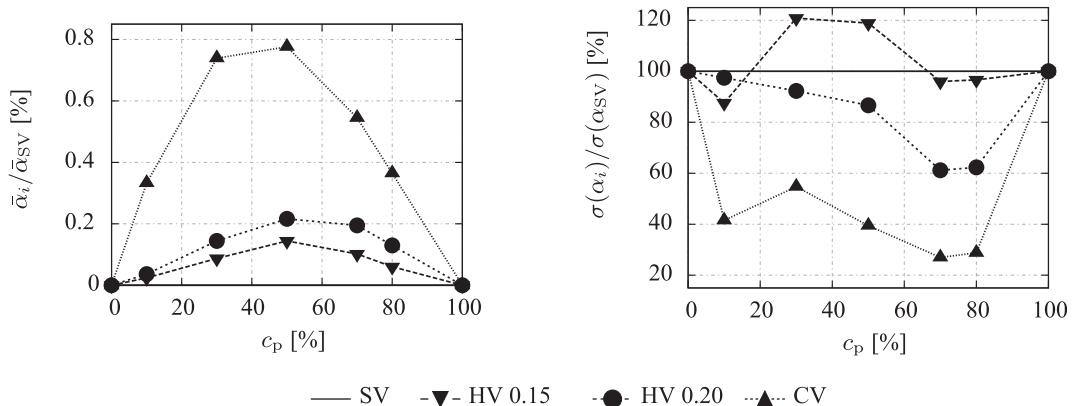

Fig. 20. Comparison of the effective isotropic thermal expansion coefficient $\bar{\alpha}_i/\bar{\alpha}_{\text{SV}}$ (left) and its normalized standard deviation $\sigma(\alpha_i)/\sigma(\alpha_{\text{SV}})$ (right) for tessellation types HV0.15, HV0.20, CV over particle volume fraction c_p.
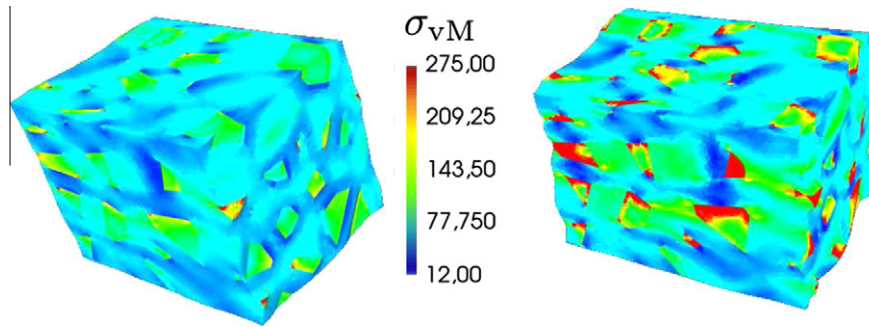
Fig. 22. Al-SiC$_p$ composite ($E_p \approx 6E_m$; left) and artificial high contrast material ($E_p = 100\ E_m$; right).

this capability. The distribution of the von Mises equivalent stress is shown in Fig. 22 for a kinematic loading of 0.1% in the $e_1 \otimes e_1$ direction for $E_p = 100E_m$ and all other parameters as stated in Table 2. Most notably, the stress concentrations at the corners of the particles are more pronounced for the near rigid particles. The authors would also like to point out that the computational time needed to solve the two phase problem with the more pronounced phase contrast (factor 16 higher) led to an increase in the solution-time of a factor of two. The chosen preconditioned conjugate gradient method can, hence, be considered as highly efficient.

5. Summary and conclusions

5.1. Summary

A method for the generation of model microstructures has been developed in Section 2 for a large class of composite materials consisting of matrix with polygonal particles using an approach similar to the early ansatz by Christoffersen (1983). The algorithm is based on the periodic Voronoi tessellation and can robustly and without additional computational effort produce microstructures containing high particle volume fractions, e.g. 80 % and more. In Section 3 the creation of a periodic spatial discretization for these materials has been described. The presented algorithm can produce arbitrarily coarse meshes without violation of the microscopic geometric properties.

The generated discretizations are used in computational homogenization problems based on the the finite element method in Section 4. The thermo-elastic material properties of Al-SiC$_p$ composites are determined for volume fractions ranging from 10 to 80%. The effect of point set constraints regularizing the Voronoi diagram has been investigated.

5.2. Conclusions

The mesh sensitivity study shows, that even for rather coarse discretizations of the geometrically and constitutionally isotropic microstructures only minor discrepancies to reference finite element calculations with very high spatial resolution can be achieved. In combination with the possibility of generating coarse discretizations based on the presented algorithm a fast method for the estimation of the effective thermo-elastic material properties of composites containing particles. Notably, the coarsest discretization (approximately 10000 nodes) considered here has the same number of degrees of freedom as a block-structured grid consisting of 20 tri-linear brick elements in each spatial direction. Such a block structured grid offers a spatial resolution of only 5% of the dimension of the unit cell. This is insufficient when taking into account that the elongation of the particles is seldom larger than

that. The proposed unstructured meshing approach can still predict the thermo-elastic properties of the material to a good extent and is, hence, favorable. Additionally, the geometry of the particles and, hence, the distribution of the stress and strain fields, are always properly represented which does not hold true for many block-structured approaches. The latter are usually based on multi-phase elements in which the different materials are distinguished integration point-wise. A modified mesh density can be realized within the particles in order to reduce the computational cost in physically non-linear calculations with elastic particles.

From the results obtained in the study of the different point sets it was found that the effective isotropic material constants are (almost) independent of the type of point seed. Taking into account that the statistical scatter is highly reduced by the centroidal type of tessellation, only a few microstructural realizations suffice to estimate the effective overall response to high precision. This reduces the computational effort considerably. A physical motivation for the centroidal Voronoi tessellation is the existence of a repulsory force acting between the particles which leads to a homogeneous distribution of the inclusion.

However, the directional anisotropy of statistical realizations depends on the shape and number of particles. Thus, the type of point seed shall not be constraint, if one is interested in the properties of particulate systems with strongly varying aspect ratios of the particles. The latter is a limiting factor for many classical homogenization schemes. For the isotropic microstructures examined in this contribution, both, the upper and lower Hashin-Shtrikman bounds are not violated for all volume fractions. Accordingly, the examined model microstructures are statistically representative.

The finite element solution predicts rather soft material behaviour, where the approximations for the bulk and shear modulus are biased versus the lower Hashin-Shtrikman estimate. The lower Hashin estimate coincides with the Mori-Tanaka estimate for the examined two phase systems, which is known to predict the elastic response of particle reinforced materials rather efficiently. Concerning the self-consistent estimate, it was found that the predictions are suitable for particle volume fractions up to approximately 30%. More investigations are needed in order to explore the inelastic material properties based on the presented microstructures in the future, where plasticity and damage will be accounted for. Another point of interest is the investigation of the statistical properties of the local stress and strain fields. The latter are subject of current investigations.

References

Aurenhammer, F., 1991. Voronoi Diagrams - A survey of a Fundamental Geometric Data Structure. ACM Computing Surveys 23, 345–405.

Barbe, F., Decker, L., Jeulin, D., Cailletaud, G., 2001. Intergranular and intragranular behavior of polycrystalline aggregates. part 1: F.e. model. International Journal of Plasticity 17, 513–536.

Barber, C., Dobkin, D., Huhdanpaa, H., 1996. The Quickhull algorithm for convex hulls. ACM Trans. Math. Softw. 22, 469–483.

Bhandari, Y., Sarkar, S., Groeber, M., Uchic, M., Dimiduk, D., Ghosh, S., 2007. 3D polycrystalline microstructure reconstruction from FIB generated serial sections for FE analysis. Computational Materials Science 41, 222–235.

Böhlke, T., Jöchen, K., Kraft, O., Löhe, D., Schulze, S., 2010. Elastic properties of polycrystalline microcomponents. Mechanics of Materials 42, 11–23.

Bollhoefer, M., Saad, Y., 2006. Multilevel preconditioners constructed from inverse-based ilus. SIAM J. Sci. Comput., Special Issue on the 8-th Copper Mountain Conference 5.

Chawla, N., Deng, X., Schnell, D., 2006a. Thermal expansion anisotropy in extruded SiC particle reinforced 2080 aluminum alloy matrix composites. Materials Science and Engineering A 426, 314–322.

Chawla, N., Deng, X., Schnell, D., 2006b. Thermal expansion anisotropy in extruded sic particle reinforced 2080 aluminum alloy matrix composites. Material Science and Engineering A 426, 314–322.

Chawla, N., Ganesh, V.V., Wunsch, B., 2004. Three-dimensional (3d) microstructure visualization and finite element modeling of the mechanical behavior of sic particle reinforced aluminum composites. Scripta Materialia 51, 161–165.

Chawla, N., Sidhu, R., Ganesh, V., 2006c. Three-dimensional visualization and microstructure-based modeling of deformation in particle-reinforced composites. Acta Materialia 54, 1541–1548.

Chawla, N., Chawla, K.K., 2006. Metal matrix composites. Springer, New York, NY.

Christoffersen, J., 1983. Bonded granulates. Journal of the Mechanics and Physics of Solids 31, 55–83.

Clyne, T.W., Withers, P.J., 1995. An introduction to metal matrix composites. Cambridge solid state science series. Cambridge University Press, Cambridge. 1. paperback ed. edition.

Decker, L., Jeulin, D., 2000. Simulation 3d de matériaux aléatoires poly-cristallins. Revue de MTtallurgie - CIT/Science et Génie des Matériaux, 271–275.

Doghri, I., Ouaar, A., 2003. Homogenization of two-phase elasto-plastic composite materials and structures study of tangent operators, cyclic plasticity and numerical algorithms. International Journal of Solids and Structures 40, 1681–1712.

Du, Q., Faber, V., Gunzburger, M., 1999. Centroidal Voronoi Tessellations: Applications and Algorithms. SIAM Review 41, 637–676.

Federov, F., 1968. Theory of Elastic Waves in Crystals. Plenum Press, New York.

Flaquer, J., Ríos, A., Martín-Meizoso, A., Nogales, S., Böhm, H., 2007. Effect of diamond shapes and associated thermal boundary resistance on thermal conductivity of diamond-based composites. Computational Materials Science 41, 156–163.

Fritzen, F., Böhlke, T., Schnack, E., 2009. Periodic three-dimensional mesh generation for crystalline aggregates based on voronoi tessellations. Computational Mechanics 43, 701.

Ganesh, V., Chawla, N., 2005. Effect of particle orientation anisotropy on the tensile behavior of metal matrix composites: experiments and microstructure-based simulation. Materials Science and Engineering A 391, 342–353.

Groeber, M., Haley, B., Uchic, M., Dimiduk, D., Ghosh, S., 2006. 3D reconstruction and characterization of polycrystalline microstructure using a FIB-SEM. Materials Characterization 57, 259–273.

Jang, W.Y., Kraynik, A., Kyriakides, S., 2008. On the microstructure of open-cell foams and its effect on elastic properties. International Journal of Solids and Structures 45, 1845–1875.

Kanit, T., Forest, S., Galliet, I., Mounoury, V., Jeulin, D., 2003. Determination of the size of the representative volume element for random composites: statistical and numerical approach. International Journal of Solids and Structures 40, 3647–3679.

Kanit, T., N'Guyen, F., Forest, S., Jeulin, D., Reed, M., Singleton, S., 2006. Apparent and effective physical properties of heterogeneous materials: Representativity of samples of two materials from food industry. Computer Methods in Applied Mechanics and Engineering 195, 3960–3982.

Kim, H., Swan, C., Lakes, R., 2002. Computational studies on high-stiffness, high-damping sic-insn particulate reinforced composites. International Journal of Solids and Structures 39, 5799–5812.

Kumar, S., Kurtz, S., 1994. Simulation of material microstructure using a 3d Voronoi tesselation: Calculation of effective thermal expansion coefficient of polycrystalline materials. Acta Metallurgica et Materialia 42, 3917–3927.

Madi, K., Forest, S., Boussuge, M., Gaillieègue, S., Lataste, E., Buffière, J.Y., Bernard, D., Jeulin, D., 2007. Finite element simulations of the deformation of fused-cast refractories based on x-ray computed tomography. Computational Materials Science 39, 224–229.

Miserez, A., Rossoll, A., Mortensen, A., 2004. Investigation of crack-tip plasticity in high volume fraction particulate metal matrix composites. Engineering Fracture Mechanics 71, 2385–2406.

Nogales, S., Böhm, H., 2008. Modeling of the thermal conductivity and thermomechanical behavior of diamond reinforced composites. International Journal of Engineering Science 46, 606–619.

Ohser, J., Mücklich, F., 2000. Statistical Analysis of Microstructures in Materials Science. Statistics in Practice. John Wiley & Sons.

Prabu, S., Karunamoorthy, L., 2008. Microstructure-based finite element analysis of failure prediction in particle-reinforced metal-matrix composite. Journal of Materials Processing Technology 207, 53–62.

Ragnemalm, I., 1992. Fast erosion and dilation by contour processing and thresholding of distance maps. Pattern Recognition Letters 13, 161–166.

Reid, A., Langer, S., Lua, R., Coffman, V., Haan, S.I., Garcia, R., 2008. Image-based finite element mesh construction for material microstructures. Computational Materials Science 43, 989–999.

Roberts, A.P., Garboczi, E.J., 2001. Elastic moduli of model random three-dimensional closed-cell cellular solids. Acta Materialia 49, 189–197.

Rosen, B.W., Hashin, Z., 1970. Effective thermal expansion coefficients and specific heats of composite materials. International Journal of Engineering Science 8, 157–173.

Shewchuk, J., 1996. Engineering a 2D Quality Mesh Generator and Delaunay Triangulator. In: Lin, M., Manocha, D. (Eds.), Applied Computational Geometry: Towards Geometric Engineering. Springer-Verlag, pp. 203–222.

Si, H., Gaertner, K., 2005. Meshing Piecewise Linear Complexes by Constrained Delaunay Tetrahedralizations, in: Proceedings of the 14th International Meshing Roundtable, pp. 147–163.

Suresh, S. (Ed.), 2002. Fundamentals of metal matrix composites. Knovel, Norwich, NY.

Torquato, S., 2002. Random heterogeneous materials: microstructure and macroscopic properties. Springer.

Willis, J., 1981. Variational and related methods for the overall properties of composites. Adv ances in Applied Mechanics, vol. 21. Elsevier. pp. 1–78.

Yue, Z.Q., Chen, S., Tham, L.G., 2003. Finite element modeling of geomaterials using digital image processing. Computers and Geotechnics 30, 375–397.

Zienkiewicz, O., Taylor, R., Zhu, J.Z., 2006. Finite element method, 6. ed., repr. edition. Butterworth-Heinemann.